ADVANCED ENERGY & SUSTAINABILITY RESEARCH
www.advenergysustres.com

Suppressed Thermal Conductivity in van der Waals Semiconductor SnS_2 by Stacking Engineering

Han Yang, Changsheng Min, Chao Li, Yuan Yu, Bangzhi Ge,* and Chongjian Zhou**

Thermal transport in crystals highly depends on the vibrations of the lattice. If the intrinsic period of the lattice is disrupted, phonon transport within the lattice will be suppressed. Herein, a strategy is reported for thermal conductivity suppression in the 2D van der Waals semiconductor SnS_2 by layer period engineering. The stacking period for SnS_2 layers is broken by mechanical alloying combined with spark plasma sintering. Double Cs-corrected transmission electron microscopy reveals that 2H and 4H SnS_2 structures coexist by stacking along the *c*-axis, demonstrating the long-range ordered but short-range disordered arrangement. As a result, the lattice thermal conductivity of SnS_2 decreases from ≈2.0 to ≈1.18 $W m^{-1} K^{-1}$ at 673 K. The strategy promises the potential application of SnS_2 in scenarios where low thermal conductivity is essential such as thermoelectric materials.

1. Introduction

Thermal energy in solids is transferred through the movement of atomic vibrations and free electrons. As a result, the total thermal conductivity (κ_{tot}) is the combined effect of lattice thermal conductivity (κ_{lat}) and electronic thermal conductivity (κ_{ele}). Lattice thermal conductivity primarily governs thermal transport in semiconductors and insulators, while electronic thermal conductivity is dominant in metals. Achieving ultralow thermal conductivity in materials is particularly valuable for addressing challenges in applications such as thermal barriers, energy conversion devices, and thermal management systems.[1,2] However, it remains a significant challenge to attain such extreme values, as κ_{lat} is intrinsically influenced by the material's structure and constituent elements, which directly impact phonon propagation and scattering.[3,4]

The lattice thermal conductivity κ_{lat} is inversely related to the phonon mean free path (l) and phonon group velocity (v_{pho}), as expressed by the equation $\kappa_{lat} = 1/3\, c_p\, l\, v_{pho}$, where c_p is the heat capacity. Traditionally, κ_{lat} has been reduced by shortening l through various phonon scattering methods such as alloying,[5–7] doping,[8,9] and creating nanostructures.[10,11] These techniques disrupt phonon transport across different frequency ranges: alloying and doping affect high-frequency phonons, while nanostructures impact low-frequency phonons. Recently, complex defect architectures with multiple scattering mechanisms have emerged as a strategy for suppressing κ_{lat}. Some novel compounds, including SnSe,[12] $K_2Bi_8Se_{13}$,[13] $TlInTe_2$,[14] $AgBi_3S_5$,[15] and CdSb,[16] display intrinsically ultralow κ_{lat} without relying on external defect structures. This behavior is attributed to strong anharmonicity in their structures and chemical bonds, which softens the crystal lattice and reduces the phonon group velocity (v_{pho}), providing an unconventional means of lowering κ_{lat}.

In addition, 2D van der Waals (vdW) or vdW-like semiconductors such as Bi_2Te_3,[17] InSe,[18] and $SnSe_2$[19] exhibit intrinsically low κ_{lat} along the perpendicular layer direction due to the presence of weak interlayer interactions. More importantly, once the interlayer periodicity is broken, the phonon transport will then be further suppressed. For example, through the spontaneous formation of $Sn_mSb_{2n}Te_{3n+m}$ heterostructures by intergrowing the Sb-rich layers within the SnTe matrix, the κ_{lat} is reduced from 2.88 $W m^{-1} K^{-1}$ in pristine SnTe to 0.8 $W m^{-1} K^{-1}$ in $Sn_{0.85}Sb_{0.15}Te$ at room temperature.[20] Compared to the lattice thermal conductivity of pure TiS_2 at 323 K, which is ≈1.67 $W m^{-1} K^{-1}$, the introduction of periodic disorder to form $(BiS)_{1.2}(TiS_2)_2$ through the alternate stacking of pure TiS_2 and BiS significantly reduces the lattice thermal conductivity to 0.65 $W m^{-1} K^{-1}$.[21]

The nontoxic, low-cost 2D vdW semiconductor SnS_2 has a layered structure and can form polytypes with nearly equal lattice energies, such as 2H, 4H, and 18R-SnS_2, according to the different stacking orders between layers.[22] Here, we report a new strategy to reduce the lattice thermal conductivity of SnS_2 by

H. Yang, C. Min, B. Ge, C. Zhou
Shenzhen Research Institute of Northwestern Polytechnical University
Sanhang Science & Technology Building
No. 45th, Gaoxin South 9th Road, Nanshan District, Shenzhen City 518057, China
E-mail: bangzhige@nwpu.edu.cn; cjzhou@nwpu.edu.cn

C. Li
The Fifth Electronics Research Institute of Ministry of Industry and Information Technology
Guangzhou 510006, China

Y. Yu
Institute of Physics (IA)
RWTH Aachen University
52074 Aachen, Germany
E-mail: yu@physik.rwth-aachen.de

The ORCID identification number(s) for the author(s) of this article can be found under https://doi.org/10.1002/aesr.202500070.

DOI: 10.1002/aesr.202500070

regulating the interlayer periodicity. The mixed 2H and 4H phases were obtained by high-energy ball milling during the mechanical alloying process. The introduction of the 4H phase disrupts the long-range periodic arrangement of the 2H phase, which enhances phonon scattering and reduces the lattice thermal conductivity to $\approx 1.18\ W\ m^{-1}\ K^{-1}$ at 673 K, a record-low value for SnS_2.

2. Results

SnS_2 exhibits a characteristic CdI_2-type layered structure, where each unit cell comprises two sheets of hexagonally close-packed S atoms, with Sn atoms occupying the octahedral voids between these S layers. Research findings indicate that SnS_2 can display multiple polytypisms, forming various crystal structures such as 2H and 4H, distinguished by increased periodicity along the *c*-axis, as illustrated in **Figure 1**a. The 2H and 4H SnS_2 structure shows a two-layer periodicity and a four-layer periodicity, respectively. As the 2H and 4H phases coexist along the *c*-axis, the periodicity between the SnS_2 layers is broken. Consequently, SnS_2 semiconductors with lower thermal conductivity can be obtained.

We synthesized SnS_2 using the strategy of mechanical alloying combined with spark plasma sintering (SPS). First, powder X-ray diffraction (PXRD) results for samples with a series of ball-milling times from 4 to 7 h are given in Figure 1b. For 4h of ball milling time, the Bragg reflection peak of the resulting powder shows a mixed phase of SnS and SnS_2, suggesting SnS_2 has not been fully synthesized yet. As the ball milling time was over 6 h, the relative intensity of the peaks of SnS_2 is significantly enhanced, indicating that more SnS_2 is synthesized with increasing ball milling time. Afterward, the powder with a ball milling time of 7 h was further densified by employing SPS. The PXRD pattern of the densified sample shown in Figure 1c is indexed as the mixed phase of the 2H and 4H polytypes of SnS_2. Some small impurity peaks are indexed to Sn_2S_3, whose content is estimated to be about 4.5 at% by refinement.

We characterized the atomic-level microstructures for identification of the periodicity of the constructed SnS_2 in **Figure 2**. The sample was observed by a double Cs-corrected transmission electron microscope (Cs-corrected TEM). The high-angle annular dark-field (HAADF) image in Figure 2a shows that the sample is composed of numerous grains with different orientations and holes. The element distribution of Figure 2a was collected by energy-dispersive spectrometer (EDS). It can be seen that except for the hole part, Sn and S elements are evenly distributed in the entire area, as shown in Figure 2b,c. The atomic compositions of Sn and S atoms in this area are 33.83% and 66.17%, respectively, which is consistent with the stoichiometric ratio of SnS_2. Figure 2d shows a representative high-magnification scanning transmission electron microscopy (STEM) image, which can obtain information on the atomic arrangement and local composition. Since Sn atoms ($Z = 50$) are heavier than S atoms ($Z = 16$), the bright atoms in the image are Sn and the dim atoms are S. Local magnification reveals the presence of 2H and 4H polytypes (the inset in Figure 2d). The selected area electron diffraction (SAED) of the area in Figure 2d is shown in Figure 2e, and two sets of diffraction spots along the [0 0 0 1] zone axis can be obtained. This result well confirms our design strategy that 2H and 4H coexist by stacking along the *c*-axis. The higher

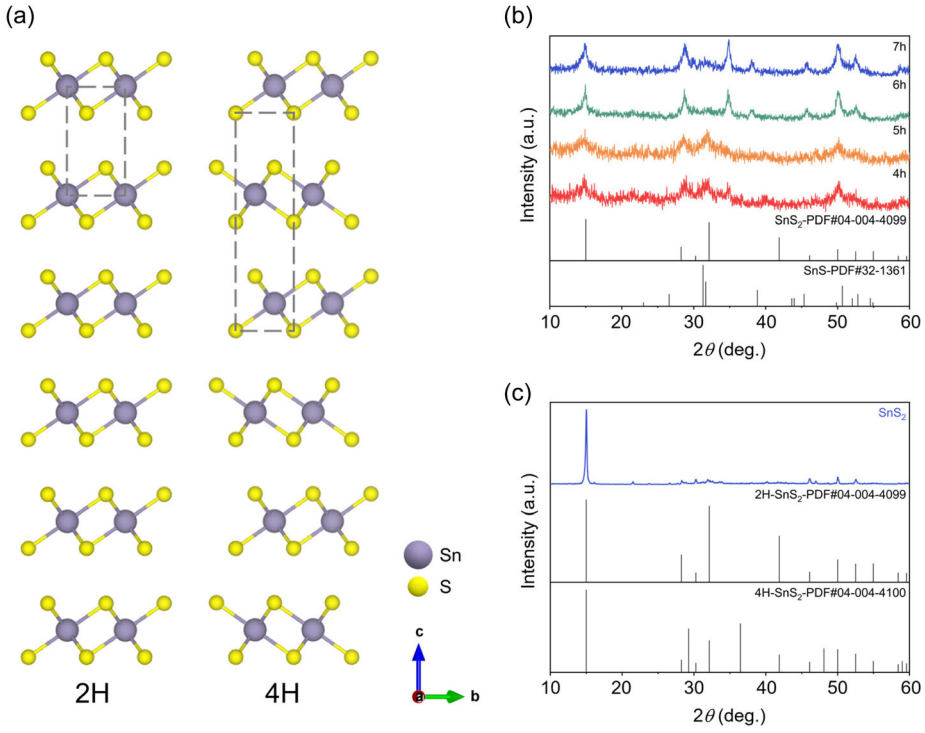

Figure 1. a) The phase structures of 2H and 4H-SnS_2 viewed along the *a*-axial direction. XRD pattern of precursor powders with b) different milling times and c) the SnS_2 bulk.

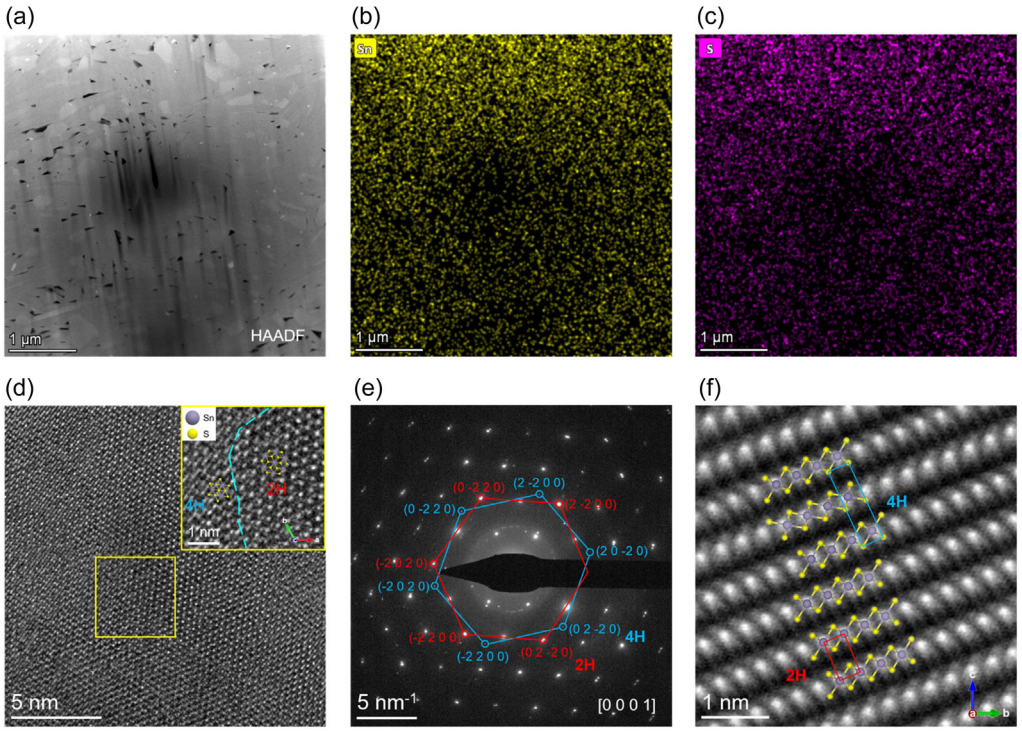

Figure 2. Microstructure of SnS_2 samples. a) Low-magnification TEM image shows the microstructure of the sample; corresponding EDS mapping for elements, b) Sn, and c) S; d) High-resolution transmission electron microscope image with contrast fluctuations. The top-right inset is an enlarged image of the yellow box area; e) SAED pattern of the area of (d); and f) atomic-resolution HAADF image.

magnification STEM image (Figure 2f) collected images of SnS_2 along the [2 −1 −1 0] zone axis, which is calibrated as mixed periodic atomic layers for 2H and 4H. Namely, the interlayer stacking cycle of SnS_2 is broken successfully via mechanical alloying combined with the SPS strategy.

We measured the total thermal conductivity (κ_{tot}) of the SnS_2 bulk in the temperature range of 350–700 K along the directions perpendicular and parallel to the SPS sintering. The κ_{tot} for the perpendicular and parallel SPS directions shows 2.98 and 1.82 $W\,m^{-1}\,K^{-1}$ at 373 K, respectively. For layered material SnS_2, the bulk sample is composed of numerous lamellar grains and has a strong texture along the vertical SPS sintering direction.[23] The significantly lower κ_{tot} in the parallel pressure direction results from phonon scattering and weaker vdW bonding in the SnS_2 interlayer. As temperature increases, the difference in κ_{tot} along these two directions gradually narrows, and reaches 1.36 and 1.18 $W\,m^{-1}\,K^{-1}$ at 673 K, respectively. The reproducibility of thermal transport properties is of fundamental importance for the reliability of results. The thermal transport properties for SnS_2 were characterized using specimens from the two independent synthesis batches (Figure S1, Supporting Information). These results demonstrate an excellent reproducibility of the experiment. The lattice thermal conductivity κ_{lat} is calculated from the formula $\kappa_{lat} = \kappa_{tot} - \kappa_{ele} = \kappa_{tot} - L\,\sigma\,T$, where L is Lorentz number (Table S1, Supporting Information).[24] The calculated κ_{lat} changes with temperature and the comparison to previously reported data for SnS_2 are shown in **Figure 3**b. From 350 to 700 K, the κ_{lat} and the κ_{tot} are almost equal, which means that the thermal transport of SnS_2 is dominated by phonon transport in the entire tested temperature range, and electrons have almost no contribution to thermal transport (Figure S2, Supporting Information). The κ_{lat} of 2.98 $W\,m^{-1}\,K^{-1}$ at 373 K in the perpendicular SPS direction is close to the reported κ_{lat} of SnS_2 without specifying the measurement direction, which is 3.13 $W\,m^{-1}\,K^{-1}$ at 373 K.[23] In contrast, the κ_{lat} parallel to the SPS direction shows a suppressed value of ≈1.18 $W\,m^{-1}\,K^{-1}$ at 673 K, much lower than that reported previously[23] over the entire measurement temperature range. To clarify the effect of different microstructures on the reduced lattice thermal conductivity, we have taken the Sn_2S_3 second phase, grain boundaries, and vacancies/nanopores into consideration in the Debye–Callaway model. Figure S3 and S4, Supporting Information demonstrate that these factors have marginal effects on the reduction in lattice thermal conductivity. Therefore, the breaking of the SnS_2 interlayer periodicity plays a significant role in suppressing the κ_{lat}.

To further understand the charge distribution in SnS_2, we first calculated the electron localization function (ELF) of 2H and 4H-SnS_2. As a robust indicator of electron pair localization, ELF allows for direct assessment of chemical interactions between neighboring atoms.[25] **Figure 4**a,b shows the ELF projected along the [1 1 −2 0] direction for 2H and 4H, respectively. The color bars from blue to red can represent the increase in electron localization. The ELF value between a part of Sn and S atoms is 0.7 ≈ 0.8, which indicates the existence of covalent bonding properties between the two, while an obvious green halo is observed

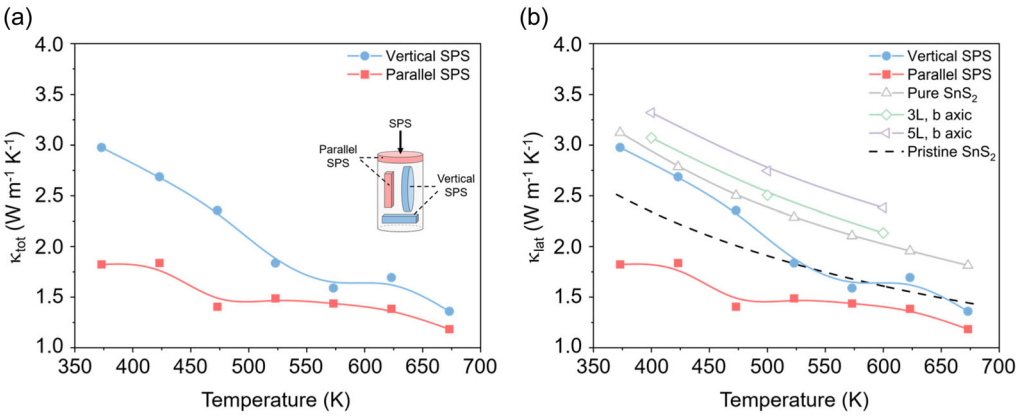

Figure 3. The thermal conductivity of SnS_2. a) The total thermal conductivity κ_{tot} and b) temperature-dependent κ_{lat} of SnS_2 in this work compared with other reported κ_{lat} of SnS_2 including pure-SnS_2,[23] 3L and 5L SnS_2,[52] and the calculated κ_{lat} of pristine SnS_2 by a Debye–Callaway model.

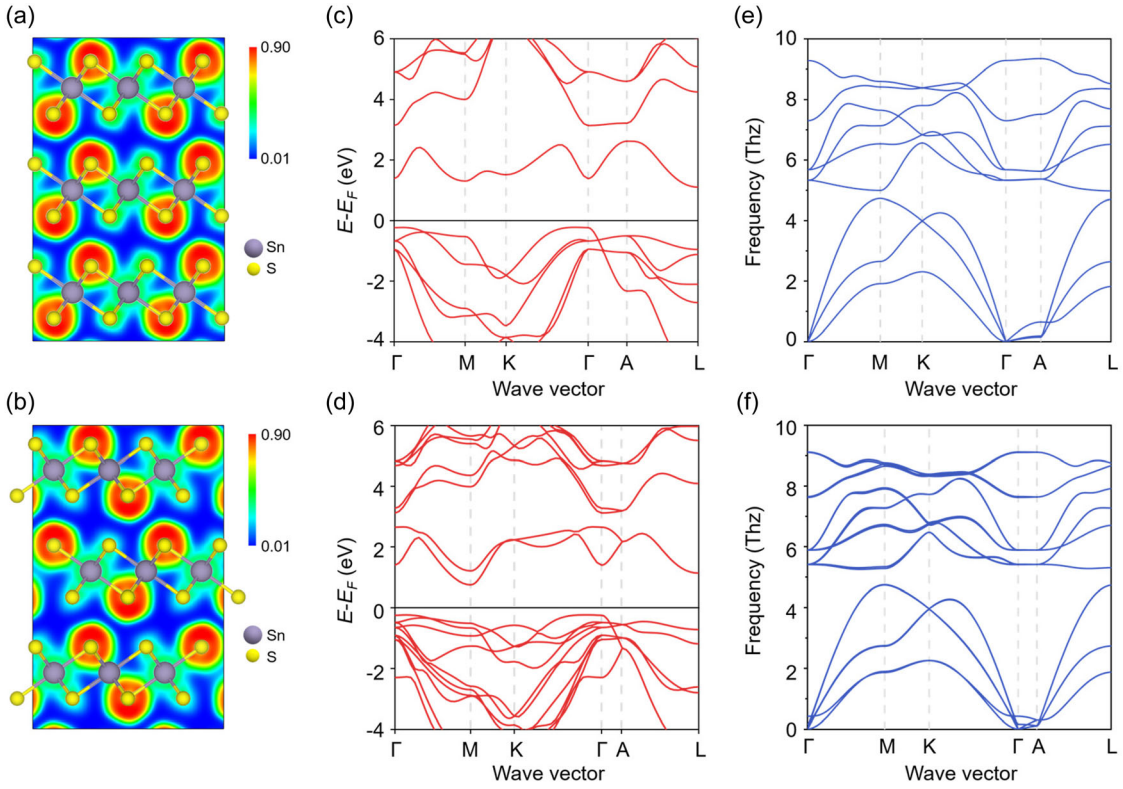

Figure 4. ELF for a) 2H and b) 4H-SnS_2; the electronic band structure of c) 2H and d) 4H-SnS_2; and the phonon spectra of e) 2H and f) 4H-SnS_2.

around another part of Sn and S atoms, with an ELF value of ≈0.4, which is consistent with the previously reported SnS_2 as an ionic-covalent crystal.[26]

Since the electronic band structure near the Fermi level has a great influence on the electrical transport properties of the material, we calculated the electronic band structure of 2H and 4H-SnS_2 as shown in Figure 4c,d, respectively. The electronic band structures show that the conduction band minimum (CBM) and valence band maximum of 2H and 4H are not in the same direction, which indicates that SnS_2 is an indirect-band semiconductor. The band structure shapes at the CBM of 2H and 4H are consistent. Consequently, when the 2H and 4H phases are mixed, the shape and position of their conduction bands do not change significantly. This suggests that multiphase mixing has minimal influence on the electrical transport properties.

As mentioned above, the thermal transport of SnS_2 is dominated by phonon transport, so we calculated the phonon spectra of 2H and 4H-SnS_2, as shown in Figure 4e,f, respectively. No negative frequencies are observed in the phonon spectrum, indicating the lattice stability of both SnS_2 phases.[27] Along the Γ–*A*

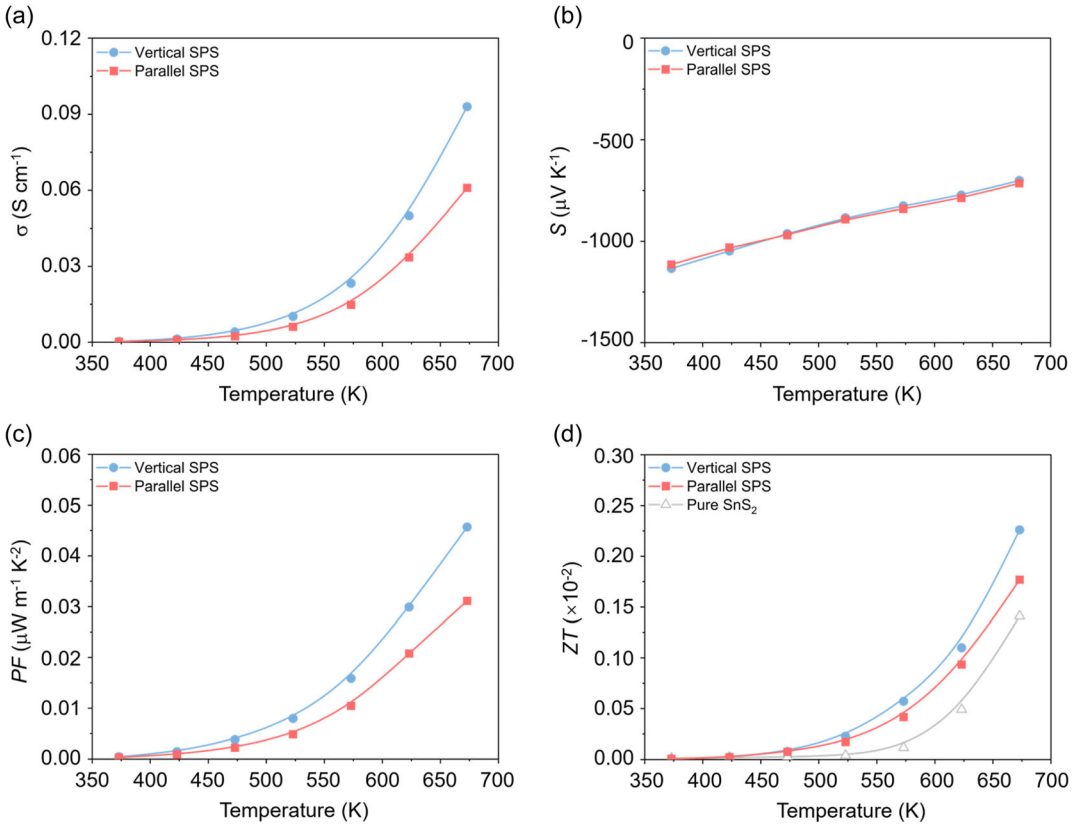

Figure 5. Thermoelectric performance of SnS_2: a) electrical conductivity; b) Seeback coefficient; c) power factor; and d) ZT.[23]

high-symmetry κ-paths, the phonon dispersion curves of the two phases are flatter than those along the Γ–K direction, which means that the phonon group velocity along the out-of-plane direction is lower than the phonon group velocity along the in-plane direction, which is related to the weak vdW interaction between layers. Meanwhile, the optical branches of the phonon spectra of both phases are much flatter than the acoustic branches, implying lower phonon group velocities.[28]

Our previous experiments and DFT have suggested that the mixed SnS_2 shows potential in suppressing κ_{lat} and maintaining charge transport, which fits the requirements of thermoelectric materials. Note that the efficiency of thermoelectric semiconductors is usually measured by the dimensionless figure of merit $ZT = S^2\sigma T/\kappa_{tot}$, where S is the Seebeck coefficient, σ is the electrical conductivity, T is the temperature (K), and κ_{tot} is the thermal conductivity, which includes the lattice thermal conductivity κ_{lat} and the electronic thermal conductivity κ_{ele}.[29–32]

We measured the electrical properties of the SnS_2 bulk in the temperature range of 350–700 K along the directions perpendicular and parallel to the SPS sintering, as shown in **Figure 5**. As the temperature increases, the electrical conductivity of the SnS_2 bulk in both test directions also shows an upward trend, showing typical semiconductor behavior (Figure 5a). The electrical conductivity in the direction perpendicular to the SPS direction increases even more, from 0.0003 S cm^{-1} at 373 K to 0.0930 S cm^{-1} at 673 K. Within the entire test temperature range, the Seeback coefficients of the SnS_2 bulk in both test directions are close (Figure 5b). The S value increases from ≈−1100 μV K^{-1} at 373 K to ≈−700 μV K^{-1} at 673 K, all of which are negative, indicating that SnS_2 is an n-type semiconductor due to the intrinsic S vacancy.[33,34] The power factor is calculated by the formula $PF = S^2\sigma$ (Figure 5c). The resulting value of PF in the perpendicular SPS direction is 0.046 μW m^{-1} K^{-2} at 673 K. Figure 5d shows the variation of the ZT value of the SnS_2 bulk with temperature. Although the electrical conductivity of the SnS_2 bulk is extremely low, by reducing the lattice thermal conductivity, its ZT value is 1.6 times higher than that of the single-phase SnS_2.[23] Further enhancements of ZT can be expected by tuning the charge carrier concentration through doping.

3. Conclusion

Lattice thermal conductivity plays a key role in thermal transport within semiconductors and insulators. Achieving small κ_{lat} is particularly important for addressing challenges in areas like thermal barriers, energy conversion systems, and thermal management. In crystalline materials, thermal transport is largely driven by lattice vibrations, and breaking the inherent periodicity of the lattice can effectively reduce phonon transport. We display a strategy for κ_{lat} suppression in the vdW semiconductor SnS_2 by engineering the layer stacking period. The stacking structure of SnS_2 layers is disrupted through mechanical alloying combined with SPS. Cs-STEM revealed a coexistence of 2H and 4H phases

along the *c*-axis, showing long-range ordered but short-range disordered arrangements. Subsequently, the κ_{lat} of SnS_2 decreases to around 1.18 $W\,m^{-1}\,K^{-1}$ at 673 K. This strategy offers promising prospects for SnS_2 in applications requiring low thermal conductivity, such as thermoelectric technology.

4. Experimental Section

Samples Synthesis: Sn powder (99.99%) was purchased from ZhongNuo Advanced Material (Beijing) Technology Co., Ltd., and S powder (99.999%) was purchased from Aladdin Company. The two elements were weighed according to the stoichiometric ratio and placed in a stainless steel vessel. The above operations were carried out in a glove box containing argon gas. Mechanical alloying was performed using a ball milling machine (MSK-SFM-3-II) with a ball-to-powder ratio of 30:1, maintaining a rotation speed of 600 rpm for 7 h. The as-prepared powder was consolidated via spark plasma sintering (SPS-3T-3-MIN(L), Chenhua Technology Co., China) in a graphite mold under vacuum conditions. The sintering process was conducted at 723 K for 5 min with an applied axial pressure of 50 MPa, yielding cylindrical specimens with approximate dimensions of 15 mm in thickness and 13 mm in diameter. The bulk density of the sintered samples was measured using an Archimedes densimeter (SJ-600G, Shuju Instrument Technology Co., Shanghai, China). For subsequent characterization, the densified samples were precisely sectioned using a low-speed diamond saw, with bar-shaped specimens prepared for electrical transport measurements and disk-shaped specimens for thermal property evaluations.

PXRD: All XRD patterns for samples were collected using a DX-27MINI powder X-ray diffractometer equipped with a Cu Kα ($\lambda = 1.5418$ Å) graphite monochromator, which operates at 40 kV and 13 mA (Haoyuan Instrument Co., Ltd., China). The measurement angle for the samples ranges from 10° to 60°, with a step width of 0.02°.

TEM: The samples for cross-sectional STEM were prepared into a wedge shape using a focused ion beam system (Helios G4 CX, FEI) with gallium ion milling. Before ion milling, a protective platinum layer was deposited on the specimen surface via sputtering. Structural and compositional analyses were conducted using a double Cs-corrected TEM (Themis Z, FEI) operating at 200 kV, equipped with a silicon drift detector (SDD) EDS system (Solid Angle 0.9-sr, X-MaxN 100TLE, OXFORD). STEM imaging was performed using a high-resolution CCD detector (2 × 2 k pixels) integrated with a GIF-QuantumER imaging filter (GATAN). For STEM-EDS elemental mapping, a probe size of 0.13 nm and a probe current of 40 pA were employed.

Charge Carrier Transport: The SPS-processed samples were sectioned and polished into various shapes and dimensions for the characterization of their charge and thermal transport properties. For simultaneous measurement of the Seebeck coefficient and electrical conductivity, bar-shaped specimens with dimensions of ≈12 × 3 × 3 mm^3 were prepared. These measurements were conducted using a CTA-3S system (Beijing Cryoall Science and Technology Co., Ltd., China) in a low-pressure helium atmosphere across a temperature range from room temperature to 673 K.

Thermal Conductivity: To protect the sample surface during measurements, a graphite coating was applied. Thermal diffusivity (*D*) was determined through the laser flash diffusivity method using a Linseis LFA 1000 instrument under helium flow, with measurements performed on disk-shaped samples measuring ≈13 mm in diameter and 1.0 mm in thickness. The total thermal conductivity (κ_{tot}) was then calculated through the fundamental relationship $\kappa_{tot} = D{\cdot}C_p{\cdot}\rho$, where ρ denotes the material density. The temperature-dependent specific heat capacity (C_p) was derived from the equation $C_p = (3 \times R \times N)/M\ J\,g^{-1}\,K^{-1}$, incorporating the ideal gas constant (*R*), material quantity (*N*), and molar mass (*M*). The lattice thermal conductivity (κ_{lat}) was derived using the relationship $\kappa_{lat} = \kappa_{tot} - \kappa_{ele} = \kappa_{tot} - L\sigma T$, where *L* is the Lorenz number, estimated based on a single parabolic band model, and σ denotes the electrical conductivity.

First-Principle Calculations: All of the first-principle calculations were based on the Vienna Ab initio Simulation Package (VASP).[35] The interaction between ions and valence electrons was described by projected augmented wave,[36] and the exchange–correlation interaction was described by the Perdew–Burke–Ernzerhof generalized gradient approximation.[37,38] The cutoff energy was set as 450 eV, and the convergence criteria for self-consistent electronic energy and residual force were respectively assumed to be 10^{-6} eV $atom^{-1}$ and 0.01 eV $Å^{-1}$, which could ensure sufficient accuracy. The *k* points are set to 9 × 9 × 4 based on Monkhorst–Pack meshes for all SnS_2-type structures in the *P*-3*m*1 and $P6_3mc$ phases. For band structure calculations, the paths of the Brillouin zone were set up based on previous work,[39] and the results of the projected band structures were obtained using the VASPKIT. The visualization of the ELF was performed using VESTA.[40]

The crystal's periodic solution was modeled using Bloch states with a Γ-centered[41] grid of 15 × 15 × 15 and a plane-wave energy cutoff of 500 eV, ensuring force convergence below 0.01 eV $Å^{-1}$ and energy convergence below 0.1 meV. For molecular dynamics simulations, a 4 × 4 × 4 supercell of the primitive cell was utilized within the canonical ensemble, employing a Nosè–Hoover thermostat. A supercell was designed with a stoichiometric ratio of 1:2 between Sn and S. The simulations were carried out over 10 ps with a time step of 1 fs at 300 K, using a plane-wave cutoff of 500 eV. The molecular dynamics data, including forces and displacements, were used to extract renormalized force constants at finite temperatures using the TDEP package.[42–44] The cutoff radii for second- and third-order force constants were set to 8 and 6 Å, respectively. Thermal conductivity was calculated using the Phono3py package,[45–47] with a converged *q*-mesh of 16 × 16 × 16. The force constants were converted from TDEP format using custom in-house scripts for this purpose.[48]

Calculation of Temperature-Dependent κ_{lat} Based on the Modified Debye–Callaway Model: The lattice thermal conductivity (κ_{lat}) as a function of temperature was calculated through the modified Debye–Callaway model expressed by Equation (1)

$$\kappa_{lat} = \frac{k_B}{2\pi^2 v}\left(\frac{k_B T}{\hbar}\right)^3 \int_0^{\theta_D} \tau_{tot}(x)\frac{x^4 e^x}{(e^x-1)^2}\,dx \tag{1}$$

where *v* is the average sound speed, θ_D is the Debye temperature, τ_{tot} is the total phonon scattering relaxation time, *x* is defined as $\hbar\omega/k_BT$, and ω is the phonon frequency.

v can be calculated

$$\frac{1}{v^3} = \frac{1}{3v_L^3} + \frac{2}{3v_T^3} \tag{2}$$

v_L and v_T are the longitudinal and transverse sound velocities, respectively.

θ_D can be calculated

$$\theta_D = \frac{\hbar}{k_B}\left(\frac{6\pi^2}{\Omega}\right)^{1/3} v \tag{3}$$

The phonon scattering relaxation time for the respective mechanism can be expressed as follows:

Umklapp phonon scattering

$$\tau_U^{-1} = A_N \frac{2}{(6\pi^2)^{1/3}}\frac{k_B \overline{V}^{1/3}\Upsilon^2\omega^2}{\overline{M}v^3} \tag{4}$$

Here, $\overline{V}$ and γ are the volume per atom and Grüneisen parameter, respectively.

Precipitates scattering

$$\tau_P^{-1} = v(\sigma_l^{-1} + \sigma_s^{-1})^{-1} V_P \tag{5}$$

Here, the scattering cross section in short- and long-wavelength regimes are $\sigma_s = 2\pi R^2$ and $\sigma_l = \frac{4}{9}\pi R^2(\Delta D/D)^2(\omega R/v)^4$, respectively;

D and ΔD are the mass density of the matrix and the difference between the particles and matrix; V_P is the number density of the particle phase.

The data used for calculations are taken from previous work.[49–51]

Calculation of Lorenz Number: Lorenz number (L) can be approximated by the Equation (6) and (7)

$$L = \left(\frac{k_B}{e}\right)^2 \left[\frac{^2F^1_{-2}}{^0F^1_{-2}} - \left(\frac{^1F^1_{-2}}{^0F^1_{-2}}\right)^2\right] \tag{6}$$

$$^nF^m_k = \int_0^\infty \left(-\frac{\partial f}{\partial \varepsilon}\right) \varepsilon^n (\varepsilon + \alpha\varepsilon^2)^m [(1+2\alpha\varepsilon)^2 + 2]^{k/2} d\varepsilon \tag{7}$$

In the equations, e is the elementary positive charge and α is the reciprocal reduced bandgap given by k_BT/E_g, in which E_g is the bandgap.

Supporting Information

Supporting Information is available from the Wiley Online Library or from the author.

Acknowledgements

C.Z. acknowledges the support from the National Key Research and Development Program of China (grant no. 2024YFA1210400), the National Natural Science Foundation of China (grant no. 22379124), the National Science Fund for Excellent Young Scientist Fund Program (Overseas) of China, and Research Fund of the State Key Laboratory of Solidification Processing (NPU) (China 2023-QZ-01), the Fund for State Key Laboratory (grant no. 6142806230202), and Guangdong Basic and Applied Basic Research Foundation (grant no. 2024A1515011165). B.G. thanks the support from the China Postdoctoral Science Foundation (Certificate Number: 2024M764249) and the Research Fund of the State Key Laboratory of Solidification Processing (NPU), China (grant no. 2024-BJ-01).

Conflict of Interest

The authors declare no conflict of interest.

Author Contributions

Han Yang: data curation (equal); formal analysis (equal); investigation (equal); writing—original draft (equal). **Changsheng Min**: data curation (equal); formal analysis (equal); validation (equal); visualization (equal). **Chao Li**: data curation (equal); formal analysis (equal); resources (equal); visualization (equal). **Yuan Yu**: conceptualization (equal); formal analysis (equal); project administration (equal); writing—review & editing (equal). **Bangzhi Ge**: conceptualization (equal); formal analysis (equal); funding acquisition (equal); supervision (equal); writing—original draft (lead). **Chongjian Zhou**: conceptualization (equal); formal analysis (equal); funding acquisition (equal); project administration (equal); supervision (equal); writing—review & editing (equal). Han Yang and Changsheng Min contributed equally to this work.

Data Availability Statement

The data that support the findings of this study are available from the corresponding author upon reasonable request.

Keywords

low thermal conductivity, SnS_2, stacking engineering, thermoelectric

Received: February 25, 2025
Revised: April 3, 2025
Published online:

[1] X. Xu, J. Chen, J. Zhou, B. Li, *Adv. Mater.* **2018**, *30*, e1705544.
[2] P. Jood, M. Ohta, A. Yamamoto, M. G. Kanatzidis, *Joule* **2018**, *2*, 1339.
[3] C. Zhou, Y. K. Lee, J. Cha, B. Yoo, S. P. Cho, T. Hyeon, I. Chung, *J. Am. Chem. Soc.* **2018**, *140*, 9282.
[4] T. Ghosh, M. Dutta, D. Sarkar, K. Biswas, *J. Am. Chem. Soc.* **2022**, *144*, 10099.
[5] Z.-Z. Luo, S. Hao, X. Zhang, X. Hua, S. Cai, G. Tan, T. P. Bailey, R. Ma, C. Uher, C. Wolverton, V. P. Dravid, Q. Yan, M. G. Kanatzidis, *Energy Environ. Sci.* **2018**, *11*, 3220.
[6] H. Pang, Y. Qiu, D. Wang, Y. Qin, R. Huang, Z. Yang, X. Zhang, L. D. Zhao, *J. Am. Chem. Soc.* **2021**, *143*, 8538.
[7] J. Yu, C. Fu, Y. Liu, K. Xia, U. Aydemir, T. C. Chasapis, G. J. Snyder, X. Zhao, T. Zhu, *Adv. Energy Mater.* **2017**, *8*, 1701313.
[8] M. Liu, M. Guo, H. Lyu, Y. Lai, Y. Zhu, F. Guo, Y. Yang, K. Yu, X. Dong, Z. Liu, W. Cai, M. Wuttig, Y. Yu, J. Sui, *Nat. Commun.* **2024**, *15*, 8286.
[9] H. Hu, Y. Ju, J. Yu, Z. Wang, J. Pei, H. C. Thong, J. W. Li, B. Cai, F. Liu, Z. Han, B. Su, H. L. Zhuang, Y. Jiang, H. Li, Q. Li, H. Zhao, B. P. Zhang, J. Zhu, J. F. Li, *Nat. Mater.* **2024**, *23*, 527.
[10] C. Chen, Z. Feng, H. Yao, F. Cao, B. H. Lei, Y. Wang, Y. Chen, D. J. Singh, Q. Zhang, *Nat. Commun.* **2021**, *12*, 5718.
[11] R. Deng, X. Su, Z. Zheng, W. Liu, Y. Yan, Q. Zhang, V. P. Dravid, C. Uher, M. G. Kanatzidis, X. Tang, *Sci. Adv.* **2018**, *4*, eaar5606.
[12] L. D. Zhao, S. H. Lo, Y. Zhang, H. Sun, G. Tan, C. Uher, C. Wolverton, V. P. Dravid, M. G. Kanatzidis, *Nature* **2014**, *508*, 373.
[13] Y. Pei, C. Chang, Z. Wang, M. Yin, M. Wu, G. Tan, H. Wu, Y. Chen, L. Zheng, S. Gong, T. Zhu, X. Zhao, L. Huang, J. He, M. G. Kanatzidis, L. D. Zhao, *J. Am. Chem. Soc.* **2016**, *138*, 16364.
[14] M. K. Jana, K. Pal, A. Warankar, P. Mandal, U. V. Waghmare, K. Biswas, *J. Am. Chem. Soc.* **2017**, *139*, 4350.
[15] G. Tan, S. Hao, J. Zhao, C. Wolverton, M. G. Kanatzidis, *J. Am. Chem. Soc.* **2017**, *139*, 6467.
[16] S. Wang, J. Yang, L. Wu, P. Wei, J. Yang, W. Zhang, Y. Grin, *Chem. Mater.* **2015**, *27*, 1071.
[17] Y. Cheng, O. Cojocaru-Mirédin, J. Keutgen, Y. Yu, M. Küpers, M. Schumacher, P. Golub, J. Y. Raty, R. Dronskowski, M. Wuttig, *Adv. Mater.* **2019**, *31*, 1904316.
[18] A. Rai, V. K. Sangwan, J. T. Gish, M. C. Hersam, D. G. Cahill, *Appl. Phys. Lett.* **2021**, *118*, 073101.
[19] P. Xiao, E. Chavez-Angel, S. Chaitoglou, M. Sledzinska, A. Dimoulas, C. M. Sotomayor Torres, A. El Sachat, *Nano Lett.* **2021**, *21*, 9172.
[20] A. Banik, B. Vishal, S. Perumal, R. Datta, K. Biswas, *Energy Environ. Sci.* **2016**, *9*, 2011.
[21] C. Wan, Y. Wang, W. Norimatsu, M. Kusunoki, K. Koumoto, *Appl. Phys. Lett.* **2012**, *100*, 101913.
[22] S. Zhan, L. Zheng, Y. Xiao, L.-D. Zhao, *Chem. Mater.* **2020**, *32*, 10348.
[23] Y. Chang, M. Ruan, F. Li, Z. Zheng, Y. Chen, Z. Ge, P. Fan, *J. Mater. Sci.: Mater. Electron.* **2020**, *31*, 5425.
[24] X. Qian, J. Zhou, G. Chen, *Nat. Mater.* **2021**, *20*, 1188.
[25] C. Zhou, Y. Yu, X. Zhang, Y. Cheng, J. Xu, Y. K. Lee, B. Yoo, O. Cojocaru-Mirédin, G. Liu, S. P. Cho, M. Wuttig, T. Hyeon, I. Chung, *Adv. Funct. Mater.* **2019**, *30*, 1908405.
[26] Z.-Q. Zhen, H.-Y. Wang, *Acta Phys. Pol. A* **2020**, *137*, 1095.
[27] Y. Huang, J. Zhou, G. Wang, Z. Sun, *J. Am. Chem. Soc.* **2019**, *141*, 8503.

[28] H. Wang, Y. Gao, G. Liu, *RSC Adv.* **2017**, *7*, 8098.
[29] Y. Yu, M. Cagnoni, O. Cojocaru-Mirédin, M. Wuttig, *Adv. Funct. Mater.* **2019**, *30*, 1904862.
[30] J. Zhang, D. Wu, D. He, D. Feng, M. Yin, X. Qin, J. He, *Adv. Mater.* **2017**, *29*, 1703148.
[31] Y. Wang, L. Yang, X. L. Shi, X. Shi, L. Chen, M. S. Dargusch, J. Zou, Z. G. Chen, *Adv. Mater.* **2019**, *31*, e1807916.
[32] W. G. Zeier, A. Zevalkink, Z. M. Gibbs, G. Hautier, M. G. Kanatzidis, G. J. Snyder, *Angew. Chem. Int. Ed. Engl.* **2016**, *55*, 6826.
[33] Y. Gong, H. Yuan, C. L. Wu, P. Tang, S. Z. Yang, A. Yang, G. Li, B. Liu, J. van de Groep, M. L. Brongersma, M. F. Chisholm, S. C. Zhang, W. Zhou, Y. Cui, *Nat. Nanotechnol.* **2018**, *13*, 294.
[34] J. H. Ahn, M. J. Lee, H. Heo, J. H. Sung, K. Kim, H. Hwang, M. H. Jo, *Nano Lett.* **2015**, *15*, 3703.
[35] G. Kresse, J. F. Èller, *Phys. Rev. B* **1996**, *54*, 11169.
[36] P. E. Blochl, *Phys. Rev. B Condens Matter.* **1994**, *50*, 17953.
[37] G. C. John, V. A. Singh, *Phys. Rev. B* **1996**, *54*, 16533.
[38] J. P. Perdew, K. Burke, M. Ernzerhof, *Phys. Rev. Lett.* **1996**, *77*, 3865.
[39] W. Setyawan, S. Curtarolo, *Comput. Mater. Sci.* **2010**, *49*, 299.
[40] V. Wang, N. Xu, J.-C. Liu, G. Tang, W.-T. Geng, *Comput. Phys. Commun.* **2021**, *267*, 108033.
[41] H. J. Monkhorst, J. D. Pack, *Phys. Rev. B* **1976**, *13*, 5188.
[42] O. Hellman, I. A. Abrikosov, *Phys. Rev. B* **2013**, *88*, 144301.
[43] O. Hellman, I. A. Abrikosov, S. I. Simak, *Phys. Rev. B* **2011**, *84*, 180301.
[44] O. Hellman, P. Steneteg, I. A. Abrikosov, S. I. Simak, *Phys. Rev. B* **2013**, *87*, 104111.
[45] L. Chaput, *Phys. Rev. Lett.* **2013**, *110*, 265506.
[46] A. Togo, L. Chaput, I. Tanaka, *Phys. Rev. B* **2015**, *91*, 094306.
[47] A. Togo, *J. Phys. Soc. Jpn.* **2023**, *92*, 012001.
[48] J. Li, L. Wei, Z. Ti, L. Ma, Y. Yan, G. Zhang, P.-F. Liu, *Phys. Rev. B* **2023**, *108*, 224302.
[49] K. G. Prasad, S. K. Kannam, S. P. Sathian, *Physica B* **2019**, *556*, 97.
[50] S. A. Bahadori, Z. Shomali, *Case Stud. Therm. Eng.* **2024**, *57*, 104377.
[51] D. Feng, F. Zheng, D. Wu, M. Wu, W. Li, L. Huang, L.-D. Zhao, J. He, *Nano Energy* **2016**, *27*, 167.
[52] J. Li, J. Shen, Z. Ma, K. Wu, *Sci. Rep.* **2017**, *7*, 8914.